International Journal of Computational Methods
Vol. 12, No. 1 (2015) 1350090 (25 pages)

DOI: 10.1142/S0219876213500904

A FAST MULTIPOLE BOUNDARY ELEMENT METHOD FOR THREE-DIMENSIONAL HALF-SPACE ACOUSTIC WAVE PROBLEMS OVER AN IMPEDANCE PLANE

HAIJUN WU*, YIJUN LIU†, WEIKANG JIANG*,§ and WENBO LU‡

*State Key Laboratory of Mechanical System and Vibration
Shanghai Jiao Tong University Shanghai 200240, P. R. China

†Mechanical Engineering, University of Cincinnati
Cincinnati, Ohio 45221-0072, USA

‡Shanghai Marine Equipment Research Institute
Shanghai 200031, P. R. China
§wkjiang@sjtu.edu.cn

Received 14 September 2012
Accepted 21 August 2013
Published 31 October 2013

A high-frequency fast multipole boundary element method (FMBEM) based on the Burton–Miller formulation is proposed for three-dimensional acoustic wave problems over an infinite plane with impedance boundary conditions. The Green's function for the sound propagation over an impedance plane is employed explicitly in the boundary integral equation (BIE). To deal with the integral appearing in the half-space Green's function, the downward pass in the FMBEM is divided into two parts to compute contributions from the real domain to the real and image domains, respectively. A piecewise analytical method is proposed to compute the moment-to-local (M2L) translator from the real domain to the image domain accurately. An algorithm based on the multi-level tree structure is designed to compute the M2L translators efficiently. Correspondingly, the direct coefficient can also be computed efficiently by taking advantage of the algorithm of the efficient M2L. A flexible generalized minimal residual (fGMRES) is applied to accelerating the solution when the convergence is very slow. Numerical examples are presented to demonstrate the accuracy and efficiency of the developed FMBEM. Good solutions and high acceleration ratios compared with the conventional boundary element method clearly show the potential of the FMBEM for large-scale 3D acoustic wave problems over an infinite impedance plane which are of practical significance.

Keywords: Fast multipole boundary element method; impedance plane; acoustic wave problems; half-space domain.

1. Introduction

Due to its features of boundary discretization and automatic satisfaction of the Sommerfeld radiation condition at infinity, the boundary element method (BEM) is an efficient tool for solving exterior acoustic wave problems. The BEM is a discretized form of the boundary integral equation (BIE) method and has been well

studied and used extensively for the numerical solutions of radiation and scattering problems for full-space acoustics. The half-space BEM which has a significant practical importance has also been investigated [Seybert and Soenarko (1988); Li *et al.* (1994); Brick and Ochmann (2008)]. For the half-space BEM in acoustic simulations, the discretization of the infinite plane is removed and only the boundaries of the structure need to be discretized. The main challenge in the half-space BEM is to find a proper Green's function satisfying the half-space boundary condition. Except for the perfectly rigid or soft infinite plane [Seybert and Soenarko (1988)], no elementary expression is available to the half-space Green's function for problems over a general infinite impedance plane.

The general half-space Green's function (a solution due to a point source over an infinite impedance plane) which involves a Sommerfeld integral is not practically useful when incorporated in the BEM. Much research has been devoted to finding a simple expression of the half-space Green's function and an efficient way to compute it. A theoretical analysis of the half-space Green's function along an impedance plane was presented by Wenzel [1974], where the Green's function was separated into three parts as incident, reflected and radiated wave. Thomasson [1976] found that the exact solution of waves from a point source over an impedance boundary given by Ingard [1951] can be rewritten in terms of a single integral along a steepest-descent contour and a Hankel function which can be easily integrated numerically. An asymptotic solution of the scalar wave field due to a point source above a locally reacting plane surface was obtained by a modified saddle point method [Kawai *et al.* (1982)], which was proved more accurate than Thomasson's method [Thomasson (1976)]. Based on a technique in which the solution of the Helmholtz equation is expressed as one fold integral with an integrand identified as the solution of the heat conduction equation for an auxiliary problem, Li *et al.* [1994] used a new method to derive the Green's function for wave propagation above an impedance ground. Later on, Li and White [1996] developed a very simple method for the efficient computation of the sound field in the near region above an impedance ground. Ochmann [2004] proposed a method called complex equivalent source method to derive the half-space Green's function which is valid for the infinite plane with mass-like as well as spring-like impedance. By converting the Sommerfeld integral into two series representations, Koh and Yook [2006] proposed an exact closed-form expression of the Sommerfeld integral in the general half-space Green's function. Chen and Waubke [2010] reformulated the expression proposed by Li *et al.* [1994] to make it suitable for two-dimensional half-space problems over an infinite plane with spring-like impedance. Even though some of the approaches introduced above are efficient in computing the half-space Green's function over an infinite impedance plane compared with the direct integration method, they are still time-consuming to be applied in the BEM for solving practical and large-scale problems.

It is well-known that the fast multipole method (FMM) [Greengard and Rokhlin (1987)] can be applied to reduce the operation counts for the BEM in the matrix-vector multiplication. Many fast multipole BEM (FMBEM) approaches

to model full-space acoustic problems have been reported in the literature (see Refs. Chen *et al.* [1997], Koc and Chew [1998], Fischer *et al.* [2004], Darve and Havé [2004], Shen and Liu [2007], Chen and Chen [2004], Nemitz and Bonnet [2008], Wu *et al.* [2012a, 2012b] and Zheng *et al.* [2012], a review up to 2002 by Nishimura [2002], a up-to-date review by Liu *et al.* [2011], and a book by Liu [2009]). Although the full-space FMBEM has been studied extensively in the literature, there are few applications of FMBEM for half-space acoustic problems. Yasuda and Sakuma [2005] proposed a symmetrical FMBEM to efficiently compute the plane-symmetric acoustic problems. The technique exploited the symmetry of the coefficients matrix for plane-symmetric model to reduce the computational complexity of matrix-vector multiplication. Therefore, it can be applied to models with one, two and three symmetrical planes. Since the half-space problems of perfectly rigid and soft infinite plane can be treated as plane-symmetric problems with respect to the infinite plane when the image model is considered, the symmetric FMBEM is also useful in dealing with half-space acoustic problems. Recently, Yasuda *et al.* proposed efficient techniques in the low-frequency FMBEM for the plane-symmetric acoustic problems [Yasuda *et al.* (2012)]. Instead of using the image model in FMBEM, Bapat *et al.* [2009] developed an adaptive half-space FMBEM which applied the half-space Green's functions of perfectly rigid and soft infinite plane explicitly in the BIE formulation. Thus, only the elements on the structure are grouped in the tree structure which in turn reduces the memory and CPU by about a half. But in practical half-space acoustic problems, the impedance boundary condition on the infinite plane which has not been applied with the FMBEM is more general than the perfectly rigid and soft cases.

In this paper, the half-space FMBEM is extended to acoustic problems over an impedance half-space plane. A general half-space Green's function which can degenerate to the perfectly rigid and soft cases is used explicitly in the BIE formulation. To deal with the integral term in the half-space Green's function, the downward pass is divided into two parts which consist of contributions from the real domain to the real and image domains, respectively. A piecewise analytical method is proposed to compute the M2L translator from the real domain to the image domain accurately and an algorithm based on the multi-level tree structure is designed to compute the M2L translator efficiently.

The paper is organized as follows: Sec. 2 consists of two parts. First part gives formulations in BEM for the half-space acoustic problems; second part presents formulations of plane wave expansion of the half-space Green's function, and the formulation of the piecewise analytical M2L translator. Section 3 has three parts. First part briefly describes expressions of the FMBEM based on the plane wave expansions of the half-space Green's function. Second part describes the algorithm of the half-space FMBEM in detail. A preconditioning method is introduced in the third part. Several numerical examples are set up to demonstrate the accuracy and

efficiency of the half-space FMBEM in Sec. 4. Section 5 concludes the paper with some comments concerning the half-space FMBEM.

2. Formulations

2.1. *BIE formulation*

Consider a finite body V with boundary surface S, submerged in a semi-infinite acoustic domain E with density ρ and speed of sound c, as shown in Fig. 1. The semi-infinite domain E is bounded by an infinite plane S_0 which has a locally reacting acoustic impedance z_m and locates at $z = 0$. The infinite plane separates the whole space into a upper half-space domain ($z > 0$) where the finite body locates, and a lower half-space domain ($z < 0$). On the plane S_0, the boundary condition can be written as

$$\frac{\partial}{\partial n}\varphi(\mathbf{x}) - \gamma\varphi(\mathbf{x}) = 0, \quad \forall\, \mathbf{x} \in S_0, \tag{1}$$

and the governing equation of the time-harmonic ($e^{-i\omega t}, i = \sqrt{-1}$) acoustic wave field in domain E can be expressed as

$$\nabla^2\varphi(\mathbf{x}) + k^2\varphi(\mathbf{x}) = 0, \quad \forall\, \mathbf{x} \in E, \tag{2}$$

where γ is the acoustic admittance defined as $\gamma = ik\rho c/z_m$, ∇^2 is the Laplace operator, $\varphi(\mathbf{x})$ is the sound pressure at point $\mathbf{x}$, and k is the wave number defined by $k = \omega/c$, with ω being the angular frequency.

It is well known that harmonic acoustic wave problems can be formulated by an integral representation at an observation point $\mathbf{x}$ in domain E as follows:

$$\varphi(\mathbf{x}) = \int_S \left[G(\mathbf{x},\mathbf{y})q(\mathbf{y}) - \frac{\partial G(\mathbf{x},\mathbf{y})}{\partial n(\mathbf{y})}\varphi(\mathbf{y})\right] dS(\mathbf{y}) + \varphi^I(\mathbf{x}), \quad \forall\, \mathbf{x} \in E, \tag{3}$$

in which $q(\mathbf{y})$ is the normal gradient of sound pressure, defined as $q(\mathbf{y}) = \partial\varphi(\mathbf{y})/\partial n(\mathbf{y})$ where the unit normal vector $n(\mathbf{y})$ on boundary S is defined to point outwards from E as shown in Fig. 1. $\varphi^I(\mathbf{x})$ appears only for scattering problems. In

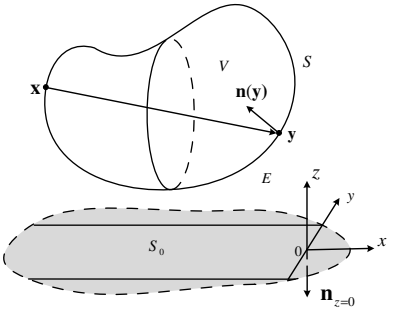

Fig. 1. Geometry of the half-space problem.

scattering problems, $\varphi^I(\mathbf{x})$ represents the incident wave (which should satisfy the half-space boundary condition, Eq. (1)), and $\varphi(\mathbf{x})$ represents the total wave which is composed of incident wave and scattering wave.

For half-space problems with a mass-like impedance infinite plane, the Green's function can be expressed as [Ochmann (2004)]

$$G(\mathbf{x},\mathbf{y}) = \frac{e^{ikr(\mathbf{x},\mathbf{y})}}{4\pi r(\mathbf{x},\mathbf{y})} + \frac{e^{ikr(\overline{\mathbf{x}},\mathbf{y})}}{4\pi r(\overline{\mathbf{x}},\mathbf{y})} + 2\gamma \int_{-\infty}^{0} e^{-\gamma\eta} \frac{e^{ikr(\overline{\mathbf{x}}+\eta\hat{\boldsymbol{z}},\mathbf{y})}}{4\pi r(\overline{\mathbf{x}}+\eta\hat{\boldsymbol{z}},\mathbf{y})} d\eta, \tag{4}$$

where $r(\mathbf{x},\mathbf{y}) = |\mathbf{x}-\mathbf{y}|$ means distance between two points $\mathbf{x}$ and $\mathbf{y}$, $\overline{\mathbf{x}}$ is the mirror point of point $\mathbf{x}$ in the lower half-space domain, and $\hat{\boldsymbol{z}} = (0,0,1)$ is a unit vector in z direction, as shown in Fig. 2. The real part of γ is less than zero ($\mathrm{Re}\{\gamma\} < 0$) which is the guarantee of convergence of the integral in the Green's function for mass-like impedance plane or physically absorbing plane. Obviously, two extreme cases that the infinite plane is rigid and soft correspond to $\gamma \to -0$ and $\gamma \to -\infty$, respectively. For spring-like impedance plane, another version of Green's function should be applied [Ochmann (2004)]. In this paper, we only consider the FMBEM for acoustic problems over the mass-like impedance plane which exists widely in engineering. The same method can be easily applied to half-space acoustic problems over a spring-like impedance plane [Ochmann (2004)].

To facilitate the derivation, the three terms appearing in the Green's function $G(\mathbf{x},\mathbf{y})$ are denoted as

$$G_1(\mathbf{x},\mathbf{y}) = \frac{e^{ikr(\mathbf{x},\mathbf{y})}}{4\pi r(\mathbf{x},\mathbf{y})}, \tag{5}$$

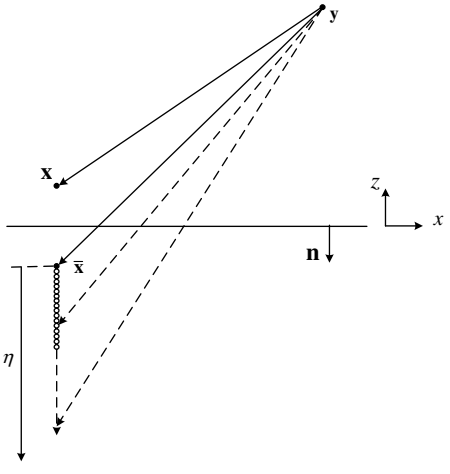

Fig. 2. Geometry of the half-space problem, the circles representing point $\overline{\mathbf{x}}+\eta\hat{\boldsymbol{z}}$ at some specific locations of η.

$$G_2(\overline{\mathbf{x}}, \mathbf{y}) = \frac{e^{ikr(\overline{\mathbf{x}}, \mathbf{y})}}{4\pi r(\overline{\mathbf{x}}, \mathbf{y})}, \tag{6}$$

$$G_3(\overline{\mathbf{x}}, \mathbf{y}) = 2\gamma \int_{-\infty}^{0} e^{-\gamma\eta} \frac{e^{ikr(\overline{\mathbf{x}}+\eta\hat{\boldsymbol{z}}, \mathbf{y})}}{4\pi r(\overline{\mathbf{x}} + \eta\hat{\boldsymbol{z}}, \mathbf{y})} d\eta. \tag{7}$$

Moving the point $\mathbf{x}$ to the boundary S will lead to a BIE. Note that the jump of the left hand side of Eq. (3) in BIE (Eq. (8)) is due to the term $G_1(\mathbf{x}, \mathbf{y})$ and free of the other two terms of the Green's function. Suppose that the boundary is discretized using N constant triangular elements ($S = \sum_{j=1}^{N} \Delta S_j$). Then, the BIE having explicit evaluation of the singular integral for acoustic problems over an impedance plane can be expressed as [Matsumoto *et al.* (2010)]

$$c(\mathbf{x}_i)\varphi(\mathbf{x}_i) + \int_{S\backslash\Delta S_i} \frac{\partial G(\mathbf{x}_i, \mathbf{y})}{\partial n(\mathbf{y})} \varphi(\mathbf{y}) dS(\mathbf{y})$$

$$= \int_{S\backslash\Delta S_i} G(\mathbf{x}_i, \mathbf{y}) q(\mathbf{y}) dS(\mathbf{y}) + \dot{\mathcal{R}}_{\mathbf{x}_i} q(\mathbf{x}_i) + \varphi^I(\mathbf{x}_i), \tag{8}$$

in which $S\backslash\Delta S_i = \sum_{j=1}^{N, j\neq i} \Delta S_j$ denotes the discretized boundary S excluding the boundary element ΔS_i on which the point $\mathbf{x}_i$ is located, and

$$c(\mathbf{x}_i) = \frac{1}{2} + \int_{\Delta S_i} \frac{\partial}{\partial n(\mathbf{y})} [G_2(\overline{\mathbf{x}}_i, \mathbf{y}) + G_3(\overline{\mathbf{x}}_i, y)] dS(\mathbf{y}), \tag{9}$$

$$\dot{\mathcal{R}}_{\mathbf{x}_i} = \dot{\alpha}(\mathbf{x}_i) + \int_{\Delta S_i} [G_2(\overline{\mathbf{x}}_i, \mathbf{y}) + G_3(\overline{\mathbf{x}}_i, \mathbf{y})] dS(\mathbf{y}), \tag{10}$$

where the constant $\dot{\alpha}(\mathbf{x}_i) = \frac{i}{2k}(1 - \frac{1}{2\pi} \sum_{m=1}^{3} \int_{\theta_1^m}^{\theta_2^m} e^{ikR(\theta)} d\theta)$. An efficient and accurate method [Wu *et al.* (2013)] is available to computing the line integral with respect to the angle θ in $\dot{\alpha}$. The configuration of the θ_1^m and $\theta_2^m (m = 1, 2, 3)$ is described in Matsumoto *et al.* [2010] and Wu *et al.* [2013].

Equation (8) is usually referred to as the conventional BIE (CBIE) which suffers from the nonuniqueness for exterior acoustic problems when the frequency coincides with the corresponding eigenfrequency of interior problems. To remove the nonuniqueness, Burton and Miller [1971] proposed a method by combining the CBIE and the normal derivative of the CBIE (HBIE). Under the condition that boundary is discretized using N constant triangular elements, the HBIE [Matsumoto *et al.* (2010)] can be expressed in the form of Eq. (8) as

$$\dot{c}(\mathbf{x}_i) q(\mathbf{x}_i) + \int_{S\backslash\Delta S_i} \frac{\partial^2 G(\mathbf{x}_i, \mathbf{y})}{\partial n(\mathbf{x}_i) \partial n(\mathbf{y})} \varphi(\mathbf{y}) dS(\mathbf{y})$$

$$= \int_{S\backslash\Delta S_i} \frac{\partial G(\mathbf{x}_i, \mathbf{y})}{\partial n(\mathbf{x}_i)} q(\mathbf{y}) dS(\mathbf{y}) + \mathcal{R}_{\mathbf{x}_i} \varphi(\mathbf{x}_i) + q^I(\mathbf{x}_i), \tag{11}$$

where

$$\dot{c}(\mathbf{x}_i) = \frac{1}{2} + \int_{\Delta S_i} \frac{\partial^2}{\partial n(\mathbf{x}_i)\partial n(\mathbf{y})}[G_2(\overline{\mathbf{x}}_i, \mathbf{y}) + G_3(\overline{\mathbf{x}}_i, \mathbf{y})]dS(\mathbf{y}), \tag{12}$$

$$\mathcal{R}_{\mathbf{x}_i} = \alpha(\mathbf{x}_i) + \int_{\Delta S_i} \frac{\partial}{\partial n(\mathbf{x}_i)}[G_2(\overline{\mathbf{x}}_i, \mathbf{y}) + G_3(\overline{\mathbf{x}}_i, \mathbf{y})]dS(\mathbf{y}), \tag{13}$$

with $\alpha(\mathbf{x}_i) = -\frac{1}{2}(ik - \frac{1}{2\pi}\sum_{m=1}^{3}\int_{\theta_1^m}^{\theta_2^m} \frac{e^{ikR(\theta)}}{R(\theta)}d\theta)$ and its computation is also described in Wu *et al.* [2013].

For an exterior ac1oustic problem, Eqs. (8) and (11) have a different set of fictitious frequencies at which a unique solution cannot be obtained. However, they will always have only one solution in common. A linear combination of Eqs. (8) and (11) (CHBIE), as given below, should give a unique solution for all frequencies:

$$\begin{aligned}[c(\mathbf{x}_i) - \beta\mathcal{R}_{\mathbf{x}_i}]\varphi(\mathbf{x}_i) + \int_{S\setminus\Delta S_i}\left[\frac{\partial G(\mathbf{x}_i, \mathbf{y})}{\partial n(\mathbf{y})} + \beta\frac{\partial^2 G(\mathbf{x}_i, \mathbf{y})}{\partial n(\mathbf{x}_i)\partial n(\mathbf{y})}\right]\varphi(\mathbf{y})dS(\mathbf{y}) \\ = [\dot{\mathcal{R}}_{\mathbf{x}_i} - \beta\dot{c}(\mathbf{x}_i)]q(\mathbf{x}_i) + \int_{S\setminus\Delta S_i}\left[G(\mathbf{x}_i, \mathbf{y}) + \beta\frac{\partial G(\mathbf{x}_i, \mathbf{y})}{\partial n(\mathbf{x}_i)}\right]q(\mathbf{y})dS(\mathbf{y}) \\ + \varphi^I(\mathbf{x}_i) + \beta q^I(\mathbf{x}_i),\end{aligned} \tag{14}$$

where β is a coupling constant that can be chosen as i/k [Kress (1985)].

Rewrite Eq. (11) in a matrix form as

$$\sum_{j=1}^{N} f_{ij}\varphi_j = \sum_{j=1}^{N} g_{ij}q_j + \varphi_i^I + \beta q_i^I, \quad \text{for node } i = 1, 2, \ldots, N, \tag{15}$$

where

$$f_{ij} = \begin{cases} \displaystyle\int_{\Delta S_j}\left[\frac{\partial G(\mathbf{x}_i, \mathbf{y})}{\partial n(\mathbf{y})} + \beta\frac{\partial^2 G(\mathbf{x}_i, \mathbf{y})}{\partial n(\mathbf{x}_i)\partial n(\mathbf{y})}\right]dS(\mathbf{y}), & i \neq j \\ \displaystyle\left[\frac{1}{2} - \beta\alpha(\mathbf{x}_i)\right] + \int_{\Delta S_i}\left(\frac{\partial}{\partial n(\mathbf{y})} - \beta\frac{\partial}{\partial n(\mathbf{x}_i)}\right) \\ \qquad \times [G_2(\overline{\mathbf{x}}_i, \mathbf{y}) + G_3(\overline{\mathbf{x}}_i, \mathbf{y})]dS(\mathbf{y}), & i = j, \end{cases} \tag{16}$$

and

$$g_{ij} = \begin{cases} \displaystyle\int_{\Delta S_j}\left[G(\mathbf{x}_i, \mathbf{y}) + \beta\frac{\partial G(\mathbf{x}_i, \mathbf{y})}{\partial n(\mathbf{x}_i)}\right]dS(\mathbf{y}), & i \neq j \\ \displaystyle\left[\dot{\alpha}(\mathbf{x}_i) - \frac{\beta}{2}\right] + \int_{\Delta Si}\left(1 - \beta\frac{\partial^2}{\partial n(\mathbf{x}_i)\partial n(\mathbf{y})}\right) \\ \qquad \times [G_2(\overline{\mathbf{x}}_i, \mathbf{y}) + G_3(\overline{\mathbf{x}}_i, \mathbf{y})]dS(\mathbf{y}), & i = j, \end{cases} \tag{17}$$

in which ΔS_j represents the triangular element j (in the case of using constant element).

Assume that the boundary conditions on the surface are:

$$\begin{cases} \varphi(\mathbf{x}) = \overline{\varphi}(\mathbf{x}), & \forall\, \mathbf{x} \in S_I, \\ q(\mathbf{x}) = \overline{q}(\mathbf{x}), & \forall\, \mathbf{x} \in S_{II}, \end{cases} \tag{18}$$

where $S = S_I \cup S_{II}$, and the barred quantities indicate given values on the boundary. By substituting boundary condition Eq. (18) into Eq. (15), and moving the unknown terms to the left-hand side and known terms to the right-hand side, Eq. (15) can be written as

$$\begin{bmatrix} a_{11} & a_{12} & \cdots & a_{1N} \\ a_{21} & a_{22} & \cdots & a_{11} \\ \vdots & \vdots & \ddots & \vdots \\ a_{N1} & a_{N2} & \ldots & a_{NN} \end{bmatrix} \begin{bmatrix} \lambda_1 \\ \lambda_1 \\ \vdots \\ \lambda_N \end{bmatrix} = \begin{bmatrix} b_1 \\ b_2 \\ \vdots \\ b_N \end{bmatrix}, \quad \text{or} \quad \mathbf{A}\boldsymbol{\lambda} = \mathbf{b}, \tag{19}$$

where $\mathbf{A}$ is the system matrix, $\boldsymbol{\lambda}$ is the unknown vector, $\mathbf{b}$ is the product of known boundary value vector and corresponding coefficient matrix plus the possible incident-wave term. It is worthy of noting that getting the system matrix in the conventional BEM approach is extremely time-consuming due to computation of the integral in the Green's function. Even though some methods were proposed to compute the Green's function efficiently [Koh and Yook (2006); Sarabandi *et al.* (2002)], the efficiency issue is still a big obstacle in applying BEM to half-space acoustic problems over an impedance plane.

To solve Eq. (19) efficiently with an iterative solver, a FMBEM is derived for half-space acoustic wave problems over an impedance plane.

2.2. *The expansion formulations*

There are generally three types of FMBEM for acoustic problems, termed as low frequency, high frequency and wideband FMBEM, respectively. The low frequency FMBEM is based on the multipole expansion [Shen and Liu (2007)] of the Green's function which is not efficient for high frequency problems. The high frequency FMBEM is based on the plane wave expansion (also referred to as the diagonal form expansion) [Rahola (1996)] of the Green's function which suffers from numerical instability for low frequency problems. The wideband FMBEM [Cheng *et al.* (2006); Gumerov and Duraiswami (2009)] is a hybrid form of the low frequency and high frequency FMBEM which is stable and efficient for wide range of frequencies. Since the multipole expansion of the low frequency form cannot handle the $G_3(\overline{\mathbf{x}}, \mathbf{y})$ term in the Green's function easily and efficiently, the expansion based on the plane wave form [Rahola (1996)] is derived in this section for the Green's function in Eq. (4).

Figure 3 illustrates the tree structure for the well separated source point $\mathbf{y}$ and field point $\mathbf{x}$. The plane wave expansions of terms $G_1(\mathbf{x}, \mathbf{y})$ and $G_2(\overline{\mathbf{x}}, \mathbf{y})$ can be

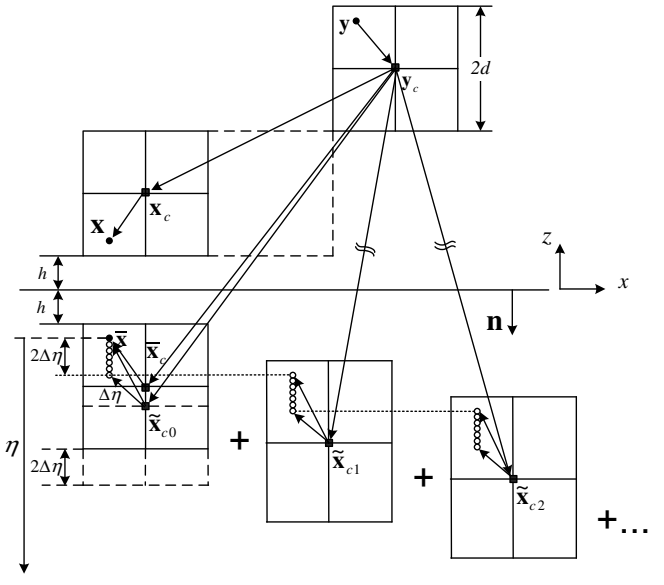

Fig. 3. Geometry of the multipole expansion.

expressed as

$$G_1(\mathbf{x},\mathbf{y}) = \frac{ik}{16\pi^2}\int_{\sigma_1} I(\hat{\boldsymbol{\sigma}},\mathbf{x},\mathbf{x}_c)T(\hat{\boldsymbol{\sigma}},\mathbf{x}_c,\mathbf{y}_c)O(\hat{\boldsymbol{\sigma}},\mathbf{y}_c,\mathbf{y})d\sigma, \tag{20}$$

$$G_2(\overline{\mathbf{x}},\mathbf{y}) = \frac{ik}{16\pi^2}\int_{\sigma_1} I(\hat{\boldsymbol{\sigma}},\overline{\mathbf{x}},\overline{\mathbf{x}}_c)T(\hat{\boldsymbol{\sigma}},\overline{\mathbf{x}}_c,\mathbf{y}_c)O(\hat{\boldsymbol{\sigma}},\mathbf{y}_c,\mathbf{y})d\sigma, \tag{21}$$

in which $\mathbf{x}_c$ is an expansion point near $\mathbf{x}$ and $\mathbf{y}_c$ is that near $\mathbf{y}$, $\overline{\mathbf{x}}$ and $\overline{\mathbf{x}}_c$ are mirror points of points $\mathbf{x}$ and $\mathbf{x}_c$, respectively. The translation, inner and outer functions in Eq. (20) are defined by

$$T(\hat{\boldsymbol{\sigma}},\mathbf{x}_c,\mathbf{y}_c) = \sum_{l=0}^{\infty} i^l(2l+1)h_l(ku)P_l(\hat{\boldsymbol{u}}\cdot\hat{\boldsymbol{\sigma}}), \tag{22}$$

$$I(\hat{\boldsymbol{\sigma}},\mathbf{x},\mathbf{x}_c) = e^{ik(\mathbf{x}-\mathbf{x}_c)\cdot\hat{\boldsymbol{\sigma}}}, \tag{23}$$

$$O(\hat{\boldsymbol{\sigma}},\mathbf{y}_c,\mathbf{y}) = e^{ik(\mathbf{y}_c-\mathbf{y})\cdot\hat{\boldsymbol{\sigma}}}, \tag{24}$$

respectively, where $u = |\mathbf{x}_c - \mathbf{y}_c|$ and $\hat{\boldsymbol{u}} = (\mathbf{x}_c - \mathbf{y}_c)/u$, P_l is the lth order Legendre function, $\hat{\boldsymbol{\sigma}} = \hat{\boldsymbol{\sigma}}(\theta,\phi) = (\sin\theta\cos\phi, \sin\theta\sin\phi, \cos\theta)$ in which θ and ϕ are polar coordinates of point $\boldsymbol{\sigma}$ on the unit sphere σ_1. The translation, inner and outer functions of Eq. (21) are same as that of Eq. (20) with $\mathbf{x}$ substituted by $\overline{\mathbf{x}}$ and $\mathbf{x}_c$ substituted by $\overline{\mathbf{x}}_c$. It should be noted that the l in Eq. (22) has to be properly truncated to avoid the numerical instability. The plane expansion for the term $G_3(\overline{\mathbf{x}},\mathbf{y})$ is not straightforward. Since there is a η-shift for $\overline{\mathbf{x}}$ in z direction in $G_3(\overline{\mathbf{x}},\mathbf{y})$, proper

shift for the local expansion center $\overline{\mathbf{x}}_c$ is needed to offset the shift of $\overline{\mathbf{x}}$. By following the plane wave expansion form of terms $G_1(\mathbf{x},\mathbf{y})$ and $G_2(\overline{\mathbf{x}},\mathbf{y})$ and reordering the integrals with respect to η and the unit sphere σ_1, $G_3(\overline{\mathbf{x}},\mathbf{y})$ can be written as

$$G_3(\overline{\mathbf{x}},\mathbf{y}) = \frac{2ik\gamma}{16\pi^2}\int_{\sigma_1}\left[\int_{-\infty}^{0} e^{-\gamma\eta} I(\hat{\boldsymbol{\sigma}},\overline{\mathbf{x}}+\eta\hat{\boldsymbol{z}},\tilde{\mathbf{x}}_c(\zeta)) T(\hat{\boldsymbol{\sigma}},\tilde{\mathbf{x}}_c(\zeta),\mathbf{y}_c)d\eta\right] \times O(\hat{\boldsymbol{\sigma}},\mathbf{y}_c,\mathbf{y})d\sigma, \tag{25}$$

in which the shifted local expansion center $\tilde{\mathbf{x}}_c(\zeta)$ is taken as

$$\tilde{\mathbf{x}}_c(\zeta) = \overline{\mathbf{x}}_c + \zeta\hat{\boldsymbol{z}}, \tag{26}$$

and ζ is a variable to be selected on condition that the plane wave expansion does exist for $G_3(\overline{\mathbf{x}},\mathbf{y})$ which implies $|\tilde{\mathbf{x}}_c(\zeta)-\mathbf{y_c}| > |(\overline{\mathbf{x}}+\eta\hat{\boldsymbol{z}}-\tilde{\mathbf{x}}_c(\zeta))+(\mathbf{y_c}-\mathbf{y})|$ for a specific or a range of η.

Obviously, if we set $\zeta=\eta$, Eq. (25) can be computed by Eq. (21) but with the translation functions defined as

$$\overline{T}(\hat{\boldsymbol{\sigma}},\overline{\mathbf{x}}_c,\mathbf{y}_c) = \int_{-\infty}^{0} e^{-\gamma\eta} T(\hat{\boldsymbol{\sigma}},\tilde{\mathbf{x}}_c(\eta),\mathbf{y}_c)d\eta. \tag{27}$$

The translator is a summation of translators from a real cell to all image cells located along a line in the mirror space below the plane. Gaussian quadrature method can be used to compute the translator. But it is either inefficient or inaccurate. To avoid the direct numerical method in computing the integral with respect to the variable η, a piecewise analytical method is proposed to compute the translator accurately.

Divide the range of η into pieces as $[-\infty,0]=\bigcup_{n=0}^{\infty}[-2(n+1)\Delta\eta,-2n\Delta\eta]$ in which $\Delta\eta$ is a positive real number. For the nth piece, the variable ζ is changed to ζ_n. As shown in Fig. 3, to ensure $|\tilde{\mathbf{x}}_c(\zeta_n)-\mathbf{y_c}| > |(\overline{\mathbf{x}}+\eta\hat{\boldsymbol{z}}-\tilde{\mathbf{x}}_c(\zeta_n))+(\mathbf{y_c}-\mathbf{y})|$ for $\forall\,\eta\in[-2(n+1)\Delta\eta,-2n\Delta\eta]$, ζ_n is set as

$$\zeta_n = -(2n+1)\Delta\eta. \tag{28}$$

Therefore, Eq. (25) can be rewritten as

$$G_3(\overline{\mathbf{x}},\mathbf{y}) = \frac{2ik\gamma}{16\pi^2}\sum_{n=0}^{\infty}\int_{-2(n+1)\Delta\eta}^{-2n\Delta\eta}\int_{\sigma_1} e^{-\gamma\eta} I(\hat{\boldsymbol{\sigma}},\overline{\mathbf{x}}+\eta\hat{\boldsymbol{z}},\tilde{\mathbf{x}}_c(\zeta_n)) \times T(\hat{\boldsymbol{\sigma}},\tilde{\mathbf{x}}_c(\zeta_n),\mathbf{y}_c)O(\hat{\boldsymbol{\sigma}},\mathbf{y}_c,\mathbf{y})d\sigma d\eta. \tag{29}$$

Substituting Eqs. (23) and (28) into Eq. (29), and using the fact $\hat{\boldsymbol{z}}\cdot\hat{\boldsymbol{\sigma}}=\cos\theta$ yields

$$G_3(\overline{\mathbf{x}},\mathbf{y}) = \frac{ik}{16\pi^2}\int_{\sigma_1} I(\hat{\boldsymbol{\sigma}},\overline{\mathbf{x}},\overline{\mathbf{x}}_c)\overline{T}(\hat{\boldsymbol{\sigma}},\overline{\mathbf{x}}_c,\mathbf{y}_c)O(\hat{\boldsymbol{\sigma}},\mathbf{y}_c,\mathbf{y})d\sigma, \tag{30}$$

where

$$\overline{T}(\hat{\boldsymbol{\sigma}}, \overline{\mathbf{x}}_c, \mathbf{y}_c) = \begin{cases} 4\Delta\eta\gamma \sum_{n=0}^{\infty} e^{ik(2n+1)\Delta\eta\cos\theta} T(\hat{\boldsymbol{\sigma}}, \tilde{\mathbf{x}}_c(\zeta_n), \mathbf{y}_c), & |\mu| = 0 \\ \frac{2\gamma}{\mu}(e^{ik\Delta\eta\cos\theta} - e^{-ik\Delta\eta\cos\theta + 2\gamma\Delta\eta}) \sum_{n=0}^{\infty} \\ \quad \times T(\hat{\boldsymbol{\sigma}}, \tilde{\mathbf{x}}_c(\zeta_n), \mathbf{y}_c) e^{2n\gamma\Delta\eta}, & |\mu| \neq 0, \end{cases} \tag{31}$$

in which $\mu = ik\cos\theta - \gamma$. Therefore, analytical translator is obtained and no integration is needed any more for the variable η in every piece. But, it should be noted that diameter of the sphere containing the image cell is $2\sqrt{(d+\Delta\eta)^2 + 2d^2}$. It is larger than the diameter of real cell, $2\sqrt{3}d$. The evaluation of $G_3(\overline{\mathbf{x}}, \mathbf{y})$ based on the plane wave expansion (Eq. (30)) is illustrated in Fig. 3 in which the local expansion center $\tilde{\mathbf{x}}_c(\zeta_n)$ is denoted as $\tilde{\mathbf{x}}_{cn}$.

To let the size of the image cell approximate to that of the real cell which will facilitate the determination of the interaction and adjacent list of an image cell, $\Delta\eta$ should be close to zero. But the smaller $\Delta\eta$ is, the more pieces are generated, which will lead to increase of the CPU time in computation of translators. To make sure that the image cell has no big difference in size by comparing with the real cell, $\Delta\eta$ should be set to a relatively small constant, such as $\Delta\eta = 0.125d$ which is the constant used in the following simulations. But, if the size of the cell is very small (deep tree structure), it is not efficient to compute the translators with Eq. (31) either since the number of pieces of η in the range $[\eta', 0]$ is very large, in which η' is the truncated lower integral limit for the variable η. To avoid this drawback, an algorithm based on the tree structure is developed to speed up computation of the translators which will be described in Sec. 3.2.

It is easy to get from the above derivation that the three terms in Green's function share the same expansion formation and just with the difference in translation functions which are favorable in the code implementation. Another advantage of the plane expansion is that normal derivative of the Green's function only results in a difference in the outer function as

$$O(\hat{\boldsymbol{\sigma}}, \mathbf{y}_c, \mathbf{y}) = -ik(\boldsymbol{n} \cdot \hat{\boldsymbol{\sigma}}) e^{ik(\mathbf{y}_c - \mathbf{y}) \cdot \hat{\boldsymbol{\sigma}}}. \tag{32}$$

3. FMBEM Algorithm of the Half-Space Acoustic Problem

With all formulas introduced in Sec. 2, we are able to construct the three-dimensional FMBEM algorithm for half-space acoustic wave problems. A flexible generalized minimum residue method (fGMRES) is used in the FMBEM to solve the equation iteratively, in which the FMM is applied to accelerating the multiplication of matrix $\mathbf{A}$ and vector $\boldsymbol{\lambda}$ (Eq. (19)).

3.1. *Formulations of moment, translation and final evaluation*

In the computation of entries, f_{ij} and g_{ij}, in the system matrix A, the lower limit of variable η in term $G_3(\overline{\mathbf{x}}, \mathbf{y})$ should be truncated to a proper number η'. A method to truncate η for a given tolerance ϵ_η is to determine a constant η' satisfying $|\gamma e^{-\gamma\eta'}| = \epsilon_\eta$. To determine the truncation number in translators, the following empirical formula [Coifman *et al.* (1993)] is applied

$$p^l = kD^l + c_0 \log(kD^l + \pi), \tag{33}$$

where D^l is the diameter of the image cell at level l, and c_0 is a number to determine the desired accuracy which is chosen as 5 in the numerical examples. The integration over the unit sphere at level l is computed by p^l-points Gaussian quadrature method in the θ direction and $2p^l$-points square quadrature in the ϕ direction [Rahola (1996)].

The moment of half-space acoustic problems is the same as that in the free-space problem and defined by

$$M(\hat{\boldsymbol{\sigma}}, \mathbf{y}_c) = \int_{\Delta S_j} O(\hat{\boldsymbol{\sigma}}, \mathbf{y}_c, \mathbf{y}) q(\mathbf{y}) dS(\mathbf{y}), \tag{34}$$

$$M(\hat{\boldsymbol{\sigma}}, \mathbf{y}_c) = -ik \int_{\Delta S_j} (\boldsymbol{n} \cdot \hat{\boldsymbol{\sigma}}) O(\hat{\boldsymbol{\sigma}}, \mathbf{y}_c, \mathbf{y}) \varphi(\mathbf{y}) dS(\mathbf{y}), \tag{35}$$

for the single and double potential, respectively. The analytical integration method [Wu *et al.* (2012a)] and anti-symmetry [Wu *et al.* (2012b)] property can be applied to computing the moment more efficiently.

To perform the M2L translation from one real cell to all image cells of one real cell at once, translators of terms $G_2(\overline{\mathbf{x}}, \mathbf{y})$ and $G_3(\overline{\mathbf{x}}, \mathbf{y})$ can be combined as

$$\widetilde{T}(\hat{\boldsymbol{\sigma}}, \overline{\mathbf{x}}_c, \mathbf{y}_c) = T(\hat{\boldsymbol{\sigma}}, \overline{\mathbf{x}}_c, \mathbf{y}_c) + \overline{T}(\hat{\boldsymbol{\sigma}}, \overline{\mathbf{x}}_c, \mathbf{y}_c), \tag{36}$$

in which $T(\hat{\boldsymbol{\sigma}}, \overline{\mathbf{x}}_c, \mathbf{y}_c)$ is expressed in Eq. (22) and $\overline{T}(\hat{\boldsymbol{\sigma}}, \overline{\mathbf{x}}_c, \mathbf{y}_c)$ is computed by Eq. (31). Correspondingly, the two set of local expansion coefficients are

$$L(\hat{\boldsymbol{\sigma}}, \mathbf{x}_c) = T(\hat{\boldsymbol{\sigma}}, \mathbf{x}_c, \mathbf{y}_c) M(\hat{\boldsymbol{\sigma}}, \mathbf{y}_c), \tag{37}$$

$$L(\hat{\boldsymbol{\sigma}}, \overline{\mathbf{x}}_c) = \widetilde{T}(\hat{\boldsymbol{\sigma}}, \overline{\mathbf{x}}_c, \mathbf{y}_c) M(\hat{\boldsymbol{\sigma}}, \mathbf{y}_c). \tag{38}$$

Since $\overline{\mathbf{x}}_c$ can be obtained from $\mathbf{x}_c$, the local expansion coefficient $L(\hat{\boldsymbol{\sigma}}, \overline{\mathbf{x}}_c)$ is assigned to the cell whose center is $\mathbf{x}_c$. The local expansion coefficients $L(\hat{\boldsymbol{\sigma}}, \mathbf{x}_c)$ and $L(\hat{\boldsymbol{\sigma}}, \overline{\mathbf{x}}_c)$ can share common memory when the downward pass is divided into two parts and evaluated separately. In the upward and downward passes, the methods used to perform M2M and L2L are described in detail in Wu *et al.* [2012a, 2012b].

The final evaluation is computed by

$$f(\mathbf{x}) = \frac{ik}{16\pi^2} \int_{\sigma_1} [I(\hat{\boldsymbol{\sigma}}, \mathbf{x}, \mathbf{x}_c) L(\hat{\boldsymbol{\sigma}}, \mathbf{x}_c) + I(\hat{\boldsymbol{\sigma}}, \overline{\mathbf{x}}, \overline{\mathbf{x}}_c) L(\hat{\boldsymbol{\sigma}}, \overline{\mathbf{x}}_c)] d\sigma. \tag{39}$$

3.2. *FMBEM algorithm*

Readers are assumed to have good knowledge of the FMBEM for acoustic problems before proceeding further for the algorithm of half space acoustics. Otherwise, please refer to tutorial references for more details about FMBEM [Sakuma and Yasuda (2002); Liu and Nishimura (2006)]. As described in Sec. 3.1, the upward pass (computation of moments and M2M translation) of the half-space FMBEM is the same as that in the full-space FMBEM. In the downward pass for the half-space problem, the L2L translation and final evaluation share the same procedure with the full-space FMBEM while the M2L translation needs more attention. To efficiently compute the M2L translations, M2L is divided into two parts: other is from the real domain to the real domain which is same as that in the full-space FMBEM, and the other is from the real domain to the image domain in which the translators involve the integral of η. Because the relative positions of interaction cells are fixed and at most 316 for the full-space FMBEM, a scheme of precomputing and storing the M2L translators to reduce the CPU time in the M2L translation was developed [Wu *et al.* (2012a, 2012b)]. From a practical point of view, it is more imperative to precompute and store the M2L translators for the half-space problems especially for the M2L translation from real cells to image cells, as indicated in Eq. (31).

A few terms are defined here to facilitate the description of the algorithm for translations from real domain to image domain. The mirror cell of one real cell centered at $\mathbf{x}_c$ is referred to as the cell centered at $\overline{\mathbf{x}}_c$. The real cell centered at $\mathbf{x}_c$ is also named as the original cell of the mirror cell. A real cell and a mirror cell are said to be adjacent cells at one level l if they have at least one common projected vertex in the *xoy* plane and the distance between their centers in z direction is less than twice of the cell's side length. A real cell and a mirror cell are well separated at level l if they are not adjacent cells but their parent cells are adjacent cells at level $l-1$. Obviously, if a real cell is a well-separated cell of one mirror cell then it is also a well-separated cell of all image cells below the mirror cell, as shown in Fig. 3. The list of all the well-separated real cells of a mirror cell at level l is called the interaction list of the mirror cell. Far cells of a mirror cell are real cells whose parent cells are not adjacent to the parent cell of the mirror cell. Since the center of the mirror cell can be obtained through its original cell, the tree structure is only created for the real domain [Bapat *et al.* (2009)]. Therefore, the interaction and adjacent lists and the local expansion coefficients of a mirror image cell are all assigned to its original cell. Definitions of those terms for cells in the real domain are same to that in the full-space FMBEM.

If mirror cell is used to represent its image cells in the determination of well-separated and adjacent real cells, the translators Eq. (31) should be evaluated with n up to an integer $N = \lfloor \eta'/2\Delta\eta \rfloor$ ("$\lfloor * \rfloor$ means *round to nearest integer*") for a well-separated real cell of a mirror cell. Correspondingly $\Delta\eta$ in the Eq. (31) should be changed to $\eta'/2N$. Since $\Delta\eta$ is level-dependent, the higher the level l is, the larger the N is. Therefore, it may be very expensive to compute the M2L translators from

a well-separated real cell to a mirror cell and all its image cells at higher level l. Since the distance from the adjacent cells of a mirror cell to image cells below the mirror cell is η-dependent, as shown in Fig. 3 at a level l, if $2h - \eta \geq d^l$ in which d^l is the length of cell's side, M2L can still be performed from adjacent cells to image cells below the mirror cell with $\eta \leq 2h - d^l$. Note that $\eta \leq 0$, define a level-dependent η^l as $\min(2h - d^l, 0)$ in which d^l is the length of cell's side at level l. In the sense of multi-level tree structure, M2L should be performed from the adjacent cells to image cells below the mirror cell with η in the range of $[\eta^{l-1}, \eta^l]$ at level l. h is said to be large enough at level l if $\eta^{l-1} = 0$. A η-dependent well-separated cell of a mirror cell is termed as an adjacent real cell of the mirror cell which is well separated from image cells below the mirror cell with η in the range of $[\eta^{l-1}, \eta^l]$. Correspondingly, the list of all the η-dependent well-separated cells of a mirror cell is called the η-dependent interaction list of the mirror cell, the η-dependent far cells of a mirror cell are real cells whose parent cells are η-dependent well-separated to the parent cell of the mirror cell. The mirror cell is also used to represent its image cells in the definition of η-dependent well-separated and far cells.

The upward pass and downward pass of the half-space FMBEM are as follows:

Upward Pass: The moments and M2M translation are same as that in the full-space FMBEM [Liu and Nishimura (2006)], but the tracing up procedure should be performed from the bottom level to root level (level 0).

Downward Pass: Firstly, perform the downward pass from the level 2 to the bottom level for cells in the real domain. It is the same procedure as that in the full-space FMBEM. Secondly, perform the downward pass from the level 0 to the bottom level for cells from the real domain to the image domain. At a level l, the following steps are carried out:

Step I: Performing the L2L translation for mirror cells if level $l > 0$ which sums contributions from all far and η-dependent far cells of the mirror cells, as shown in Fig. 4. If a cell is a leaf cell, the final evaluations of the contributions from all far and η-dependent far elements to the elements in the mirror cell are computed with Eq. (39) for G_2 and G_3. Contributions from elements in adjacent cells to the element in the cell are evaluated with direct method for G_2 and G_3. Note that G_3 is just computed with η in the range of $[\eta^l, 0]$ when h is not large enough at the level l, which is more efficient than the original range $[\eta', 0]$.

Step II: Performing the M2L translation for mirror cells if h is not large enough at the level l which sums the contributions from cells in the interaction and η-dependent interaction list. We can find further that the interaction list of a mirror cell does exist only if the original cell of its parent cell locates at the bottom layer of the tree structure in z direction, as shown in Fig. 4. Therefore, there are at most $98(7^2 \times 2)$ possible relative positions of M2L translations from real cells to mirror image cells at each level. It is permissible and favorable to precompute and store the translators for the M2L translations from real cells to mirror cells. Note that

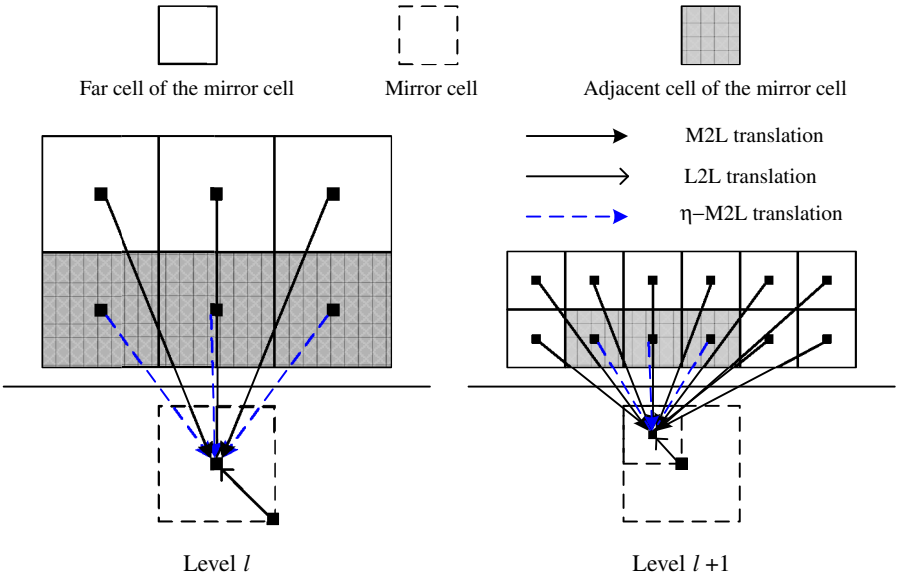

Fig. 4. (Color online) M2L and L2L from real cells to image cells, in which M2L translation covers $[\eta^l, 0]$ and η-M2L translation covers $[\eta^{l-1}, \eta^l]$ at level l for the variable η.

M2L translators of interaction list of a mirror cell consists of translators of G_2 and G_3 with η in the range of $[\eta^{l-1}, 0]$. But that of η-dependent interaction list only includes translators for G_3 with η in the range of $[\eta^{l-1}, \eta^l]$, and the translator is expressed as

$$\overline{T}(\hat{\boldsymbol{\sigma}}, \overline{\mathbf{x}}_c, \mathbf{y}_c) = \begin{cases} 4\widetilde{\Delta\eta}\gamma\gamma \displaystyle\sum_{n=0}^{\tilde{N}} e^{ik(2n+1)\beta\cos\theta} T(\hat{\boldsymbol{\sigma}}, \tilde{\mathbf{x}}_c(\zeta_n), \mathbf{y}_c), & |\mu| = 0 \\ \dfrac{2\gamma}{\mu} e^{-i\gamma\eta^l} (e^{ik\widetilde{\Delta\eta}\cos\theta} - e^{-ik\widetilde{\Delta\eta}\cos\theta + 2\gamma\beta}) \displaystyle\sum_{n=0}^{\tilde{N}} \\ \qquad \times T(\hat{\boldsymbol{\sigma}}, \tilde{\mathbf{x}}_c(\zeta_n), \mathbf{y}_c) e^{2n\gamma\widetilde{\Delta\eta}}, & |\mu| \neq 0, \end{cases} \tag{40}$$

in which $\tilde{N} = \lfloor (\eta^l - \eta^{l-1})/2\Delta\eta \rfloor$, $\widetilde{\Delta\eta} = (\eta^l - \eta^{l-1})/2\tilde{N}$ and $\zeta_n = \eta^l - (2n+1)\widetilde{\Delta\eta}$.

According to the above algorithm, there are at most 2^{2l+1} cells in the image domain needing M2L translation at level l which is smaller than the most 2^{3l} cells in the real domain from $l \geq 1$. In addition, there are at most $72(6^2 \times 2)$ M2L translations (summation of M2L and η-dependent M2L, as illustrated in the right figure in Fig. 4) from real cells to a mirror cell in contrast to the most 189 M2L translations of cell in the real domain. Therefore the CPU time cost in the downward pass for cells in the image domain is less than that for real cells. Figure 4 gives a simple explanation of the M2L, L2L translations from real cells to image cells in two dimensions.

3.3. *Preconditioning*

The coefficient matrix of the BEM is sometimes ill-conditioned, resulting in a poor rate of convergence for the solution using iterative solvers. Therefore, preconditioning for the FMBEM is crucial to its convergence and computing efficiency. To have a preconditioner for the half-space problem, a right preconditioned fGMRES [Saad (1993)] is used in which the preconditioning process is performed with the GMRES. The fGMRES satisfies the residual norm minimization property over the preconditioned Krylov subspace just as in the standard GMRES algorithm. It also enables one to utilize the memory more efficiently since the vectors that are normally not being used in a given fGMRES step can be fully exploited to compute a preconditioned vector via the inner GMRES. The tolerance of the inner GMRES is set larger than the tolerance of fGMRES. The inner GMRES solution is faster than the outer fGMRES, as the inner loop is terminated after a few iterations.

4. Numerical Examples

To the best knowledge of the authors, we are not aware of the existence of an exact analytical solution to either radiation or scattering from a sphere (or any other body) in the three-dimensional half space over an infinite impedance plane. Since FMBEM is a fast approximation to the conventional BEM (CBEM) within a given tolerance, the accuracy of the proposed FMBEM is compared with the CBEM. In the evaluation of $G_3(\overline{\mathbf{x}}, \mathbf{y})$ using direct numerical method, an exact closed-form expression [Koh and Yook (2006)] is used. It can be expressed in our symbols as

$$G_3(\overline{\mathbf{x}}, \mathbf{y}) = -\frac{\gamma}{2\pi} e^{-\gamma(z_{\mathbf{x}}+z_{\mathbf{y}})} \left\{ \pm i\pi J_0(2\sqrt{c_1 c_2}\,) + \frac{i\pi}{2}[H_0^{(2)}(2\sqrt{c_1 c_2}\,) - E_0^+(w, 2\sqrt{c_1 c_2}\,)] \right\}, \tag{41}$$

in which $z_{\mathbf{x}}$ and $z_{\mathbf{y}}$ are the z coordinates of point $\mathbf{x}$ and $\mathbf{y}$, J_0 is Bessel function of the first kind, $H_0^{(2)}$ is Hankel function of the second kind, E_0^+ is incomplete cylindrical function in Poisson form [Agrest and Maksimov (1971)], $c_1 = \frac{i}{2}(k + i\gamma)[r(\mathbf{x}, \mathbf{y}) - (z_{\mathbf{x}} + z_{\mathbf{y}})]$, $c_2 = -\frac{i}{2}(k - i\gamma)[r(\mathbf{x}, \mathbf{y}) + (z_{\mathbf{x}} + z_{\mathbf{y}})]$ and $w = \frac{\pi}{2} + iln(-\sqrt{c_2/c_1})$. In Eq. (41), the "+" is for $Re(-1/c_2) > 0$ and "−" for $Re(-1/c_2) < 0$ where Re means the real part of a complex number. There are asymptotic expansions for the three special functions in Eq. (41) but only for very special cases. In the interest of generality, Eq. (41) is used to evaluate $G_3(\overline{\mathbf{x}}, \mathbf{y})$ directly in the CBEM. It is worth noting that the exact closed-form suffers from numerical instability whenever $e^{-\gamma(z_{\mathbf{x}}+z_{\mathbf{y}})} \to +\infty$. Therefore, direct numerical quadrature [Greengard *et al.* (2011)] has to be applied in the computation of $G_3(\overline{\mathbf{x}}, \mathbf{y})$ for the case when $e^{-\gamma(z_{\mathbf{x}}+z_{\mathbf{y}})}$ is very large, such as the case $\gamma = -10^4$ in Example 4.1.

The half-space FMBEM has been implemented in a code using Fortran 95. In all examples, constant triangular elements are used in the meshing. Maximum number of elements assigned in a leaf is set to 20. 12-points Gaussian quadrature is applied

to computing the f_{ij} and g_{ij}. The tolerance ϵ_η for the determination of η' is set to 10^{-8} in all examples. The fGMRES solver is preconditioned with GMRES and will stop the iterative process when the residual reaches 10^{-4}. And the inner GMRES will stop the preconditioning process when its residual reaches 10^{-1}. The solution of the CBEM is obtained with the GMRES solver without preconditioning. All results reported below are obtained on a desktop PC with a 64-bit Intel® CoreTM2 DuoCPU and 8GBRAM, but only one core is used in the computation.

4.1. *Sphere models*

The first case is sound scattering from a sphere of radius a in close proximity to an infinite impedance plane. The distance between the infinite plane and the center of the sphere is set to $1.01a$ and $1.25a$, respectively. Acoustic admittance of the impedance plane is $\gamma = -0.914 + 0.397i$ at $ka = 2$. The surface of the sphere is assumed to be rigid. A plane wave traveling along z axis (e^{-ikz}) above the impedance plane results in $\varphi^I = e^{-ikz} + \lambda e^{ikz}$ where $\lambda = (ik - \gamma)/(ik + \gamma)$. The half-space FMBEM is compared with the CBEM in the boundary solutions. The boundary solutions of the sphere with total number of elements ranging from 1,200 to 10,000 are computed with FMBEM and CBEM.

The L2 relative error of the FMBEM with respect to CBEM are at the level of 10^{-6} which proves the accuracy of the half-space FMBEM. CPU times are plotted in Fig. 5. It clearly demonstrates the efficiency of the half-space FMBEM. The speed-up ratio of the half-space FMBEM is higher than that of the full-space one because computation of coefficients matrix in the conventional BEM is more time-consuming than that of the full space CBEM. As shown in Fig. 5, the CBEM

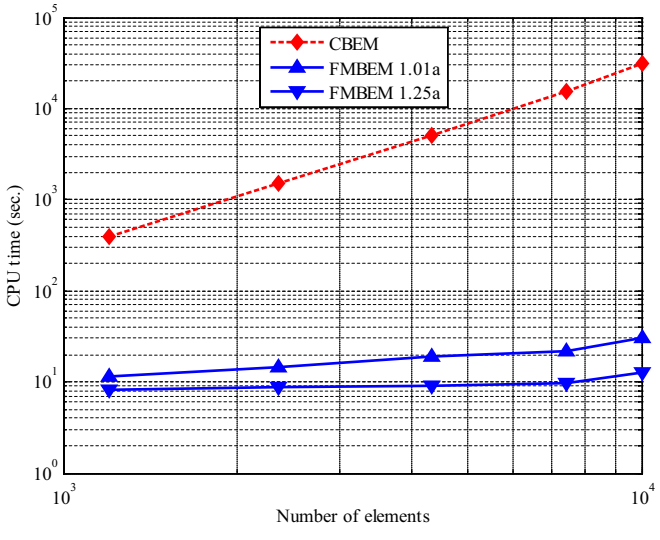

Fig. 5. (Color online) CPU time comparison between FMBEM and CBEM.

takes almost 9 h to solve the mesh with 10,000 elements and most of the time is spent on computing system matrix. It is even worse if a direct solver (such as LU decomposition method or Gaussian elimination method) is used in the CBEM. High time consumption is the reason why only meshes with number of elements less than 10,000 are used in this comparison. It is also one of the reasons why the CBEM is prevented from the analysis of half-space problems over an impedance plane even for a small model. Figure 5 illustrates that CPU time used by the FMBEM for the sphere with distance between the infinite plane and its center being $1.01a$ is more than that for the sphere with the distance being $1.25a$. It is caused by the fact that the closer the model is to the plane, the more direct coefficients between elements in the real domain and elements in the image domain involving $G_3(\overline{\mathbf{x}}, \mathbf{y})$ need to be computed.

There is no analytical result available to validate the solution of the FMBEM for large scale problems. For a model at a specific frequency, the numerical solutions given by the FMBEM should converge to the exact value by keeping refining the mesh. In this case, a plane wave is also assumed to travel along z axis (e^{-ikz}) above the impedance plane. The distance between the infinite plane and the center of the sphere is set to $1.1a$. Acoustic admittance of the impedance plane is $\gamma = -0.278 + 0.549i$. ka is chosen to be 10, 15, 20, 25, respectively. For each ka, seven different meshes varying from 6,348 to 602,112 are used to demonstrate the convergence of solutions, as shown in Fig. 6. The relative error means the error of maximum absolute sound pressures obtained with other meshes with respect to that computed with the finest mesh (number of element is 602,112). The CPU time used to solve

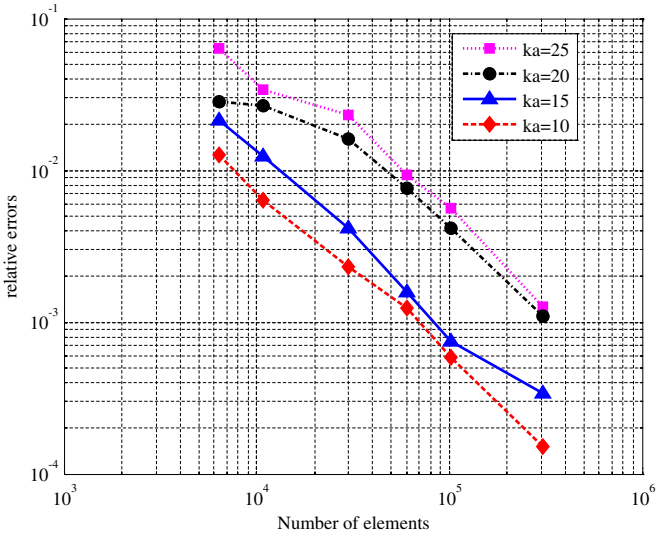

Fig. 6. (Color online) Convergence of the maximum absolute sound pressure for different ka and number of elements.

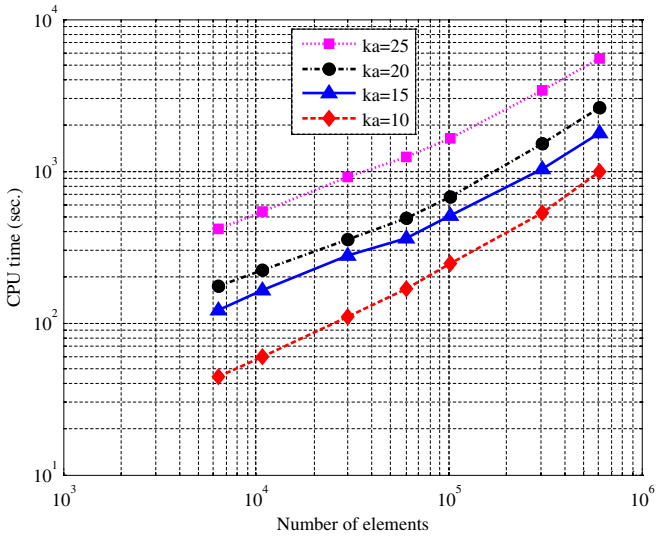

Fig. 7. (Color online) CPU time used to solve the scattering sphere for different ka and number of elements.

the problems is plotted in Fig. 7 which shows the efficiency of the FMBEM for large scale problems.

The efficiencies demonstrated in Fig. 7 are for cases when the dimensionless frequency ka is fixed while the dimensionless element size is decreasing. The FMBEM is not as efficient as that depicted in Fig. 7 if the dimensionless element sizes are fixed in meshing for different frequencies. It can be easily validated by comparing the CPU time used for the cases $ka = 20$ and $ka = 10$ in the following way. If the dimensionless element size is fixed, the element size in the case $ka = 20$ is half of that in the case $ka = 10$. Generally, one triangular element in the case $ka = 10$ will turn into four elements in the case $ka = 20$. Therefore, lines crossing the lines of $ka = 10$ and 20 in Fig. 7 with the x coordinate of intersection point with the line $ka = 20$ being four times as that of the intersection point with the line $ka = 10$ can roughly represent efficiencies of FMBEM for cases with the fixed dimensionless element size. Obviously, slopes of those lines are bigger than that shown in Fig. 7. It implicates the efficiency of the FMBEM for fixed dimensionless element size is slower. However, efficiencies of the FMBEM are amazing for both cases since the BEM can hardly be applied for practical half-space problems with an impedance plane as demonstrated in Fig. 5.

Next, we study two extreme cases using the half-space FMBEM. The distance between the infinite plane and the center of the sphere is set to $1.01a$. In this case, the sphere is assumed to pulsate with a uniform velocity at $ka = 5$. The sphere is meshed with 10,800 triangular elements. The perfectly rigid and soft cases are computed with the CBEM with the corresponding half-space Green's functions,

Table 1. Results of FMBEM for approximating the perfectly rigid and soft plane with different impedance.

Cases	Impedance γ	CPU time (Sec.)	Relative error (L2)
Perfectly rigid plane	–1.0E–02	9.898E+01	6.321E–03
	–1.0E–03	6.601E+02	6.486E–04
	–1.0E–04	4.511E+03	1.014E–04
Perfectly soft plane	–1.0E+02	3.146E+01	9.682E–02
	–1.0E+03	3.569E+01	5.332E–03
	–1.0E+04	3.555E+01	7.356E–04

$G(\mathbf{x},\mathbf{y}) = G_1(\mathbf{x},\mathbf{y}) + G_2(\overline{\mathbf{x}},\mathbf{y})$ and $G(\mathbf{x},\mathbf{y}) = G_1(\mathbf{x},\mathbf{y}) - G_2(\overline{\mathbf{x}},\mathbf{y})$, respectively. The approximation to the half space problems over perfectly rigid and soft planes by assigning to γ large numbers and small numbers, respectively (Table 1) are computed with the half-space FMBEM. Results are listed in Table 1. The relative error means the L2 relative error of the boundary solution given by FMBEM with respect to that given by CBEM. The relative errors demonstrate that the boundary solutions obtained by the half-space FMBEM do approximate to results for a perfectly rigid and soft plane by assigning to γ to their corresponding limits, as shown in Table 1. The phenomena are as expected since the perfectly soft and hard Green's functions can be obtained from Eq. (4) with γ approaching -0 and $-\infty$, respectively. It should be noted that the CPU time used by the FMBEM for perfectly soft plane is more than that for the perfectly rigid plane which is due to the different lower integral limit truncation η' for the two types of extreme impedance. To make sure $|\gamma e^{-\gamma\eta'}| = \epsilon_\eta$ for the given tolerance, $|\eta'|$ has to be very large if $|\gamma|$ is very small (such as the case $\gamma = -10^{-4}$). Therefore, it is very time-consuming to precompute the M2L translators from the real domain to the image domain.

4.2. *Scattering from multiple objects*

A scattering model of multiple objects with rigid surface located below an impedance plane is studied next. The model contains a group of 60 fish and has overall dimension of 1.0 m × 1.05 m × 0.8 m in x, y and z direction, respectively. The distance from the top of the model to the *xoy* plane as shown in Fig. 8 is 1.0 m. A plane wave traveling along z axis (e^{ikz}) below the impedance plane results in $\varphi^I = e^{ikz} + \lambda e^{-ikz}$ where $\lambda = (ik+\gamma)/(ik-\gamma)$. The dimensionless frequency ka (a is the maximum side length of the model) is 81.0. The admittance γ is $-0.104 + 0.323i$. Every fish is meshed with 8,980 triangular elements, in which the smallest triangle is 2.71×10^{-2} wavelengths, and the largest one is 8.05×10^{-2} wavelengths. So the total number of elements is 538,800. It takes 4.85 h to reach the solution with fGMRES. The boundary solution is plotted in Fig. 8. To validate the accuracy of the half-space FMBEM, a matrix-vector product is compared with CBEM. Due to the time issue, the CBEM is only applied to computing the $\mathbf{b} = \mathbf{A}_{:,1}\lambda_1$ in which $\mathbf{A}_{:,1}$ is the first row of the coefficient matrix $\mathbf{A}$ and λ_1 is the first entry of the

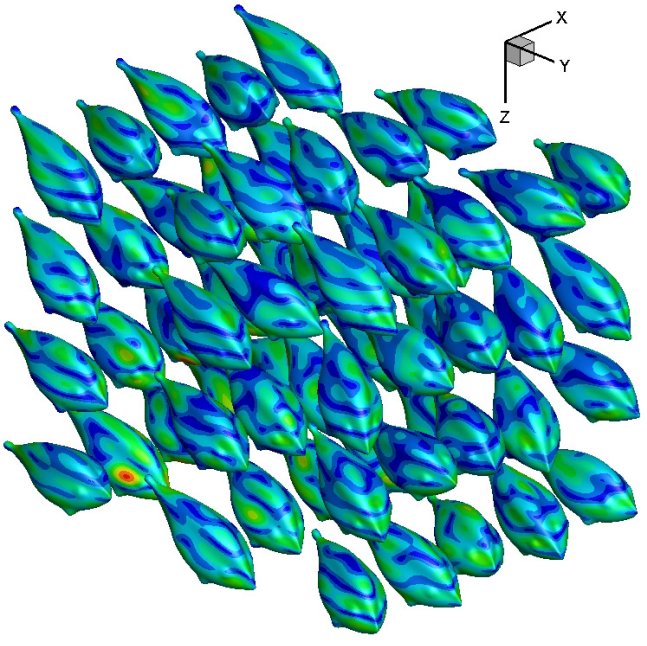

Fig. 8. (Color online) Scattering of a multiple fish model.

Table 2. CPU time and relative error of matrix-vector multiplication between the CBEM and half-space FMBEM. The CPU time used by the CBEM is extrapolated from that used in computation of $\mathbf{b} = \mathbf{A}_{:,1}\lambda_1$.

Examples	4.2		4.3	
	CBEM	FMBEM	CBEM	FMBEM
CPU time (Sec.)	7.195E+08	9.094E+01	3.516E+06	3.11E+01
Relative error (L2)	3.035E−04		2.149E−04	

unknown vector λ as shown in Eq. (19). The relative error and CPU time used in computing one matrix-vector are listed in Table 2. The relative error indicates the difference between the vector $\mathbf{b} = \mathbf{A}_{:,1}\lambda_1$ computed by the half-space FMBEM and CBEM, and the CPU time of the CBEM for one matrix-vector product equals to multiplication of the seconds used in the computation of the vector $\mathbf{b} = \mathbf{A}_{:,1}\lambda_1$ and the number of elements.

4.3. *A compressor casing model*

A compressor casing model is used to further demonstrate applicability of the half-space FMBEM. The compressor casing is excited by a unit harmonic force at $ka = 19.1$ (a is the maximum side length of the model). The boundary velocity is obtained by using a commercial FEM software. The radiating compressor

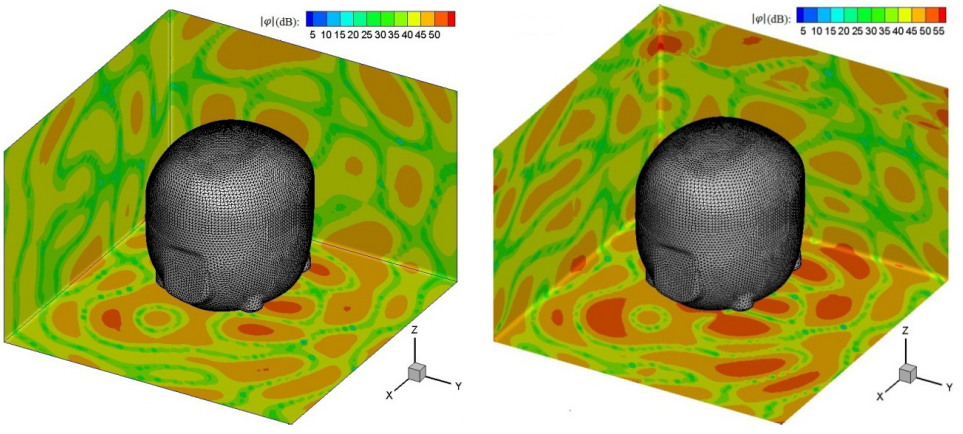

(a) (b)

Fig. 9. (Color online) Difference of the field pressure of a vibrating compressor casing computed by (a) the full-space FMBEM and (b) the half-space FMBEM.

is placed over an infinite plane with the minimum distance from the compressor to the plane being 0.025 m. The radiation of the compressor is computed by the half-space FMBEM over an impedance plane with γ being $-4.82 + 11.14i$. The compressor is meshed with 107,468 triangular elements in which the smallest triangle is 1.61×10^{-2} wavelengths, and the largest one is 4.73×10^{-2} wavelengths. The corresponding full space FMBEM is also applied to solving the same model but with the infinite plane removed to show the influence of the impedance plane on the sound pressure. Field pressure obtained by the two methods is plotted in Fig. 9. The half-space FMBEM and the full-space FMBEM takes a total of 894 and 567 seconds to get the solution, respectively. Same as the previous example, CPU time and relative error of the matrix-vector multiplication of half-space FMBEM for this case are also examined and listed in Table 2. Compared with the results obtained with the full-space FMBEM, both the distribution and maximum value of the field pressure computed with the half-space FMBEM are varied. This means the influence of the impedance plane is not negligible for this case. The problem is frequently encountered in engineering when experiments need to be set up to validate the numerical simulations which are analyzed under the free-space assumption. For these cases, the half-space FMBEM becomes useful in checking the influence of the reflecting plane on pressure at the measurement positions.

5. Conclusion and Discussion

A half-space FMBEM is developed for three-dimensional acoustic wave problems over an infinite plane with an impedance boundary condition. In the half-space FMBEM, the downward pass is divided into two parts which are used to compute the contributions from the real domain to the real and the image domains, respectively.

This makes the number of M2L from the real domain to the image domain be at most equal to 72. It is smaller than the number of 189 of M2L from the real domain to the real domain. A piecewise analytical method is proposed to compute the M2L translator from the real domain to the image domain accurately and an algorithm based on the multi-level tree structure is designed to compute the M2L translators efficiently. The level-dependent computation of the M2L translators for the cells from the real domain to the image domain is also advantageous to the computation of direct coefficient because the integral appearing in the half-space Green's function only needs to be evaluated in the range of $[\eta^l, 0]$ instead of $[\eta', 0]$ (generally $|\eta^l| \ll |\eta'|$) at level l. Numerical examples clearly demonstrate the accuracy and efficiency of the developed half-space FMBEM.

The Burton–Miller formulation is implemented in the half-space FMBEM to overcome the nonuniqueness for exterior acoustic problems. Theoretically, the half-space FMBEM based on Burton–Miller formulation should give the unique solution for all frequencies. But we cannot numerically demonstrate that, because the fictitious frequencies even for the exterior acoustic problem of a sphere over an infinite impedance plane are not clear now. Although the FMBEM algorithm introduced in this paper is based on the Green's function of the infinite plane with mass-like impedance, it can be readily modified to the half-space problems of infinite plane with spring-like impedance which has a similar Green's function [Eq. (37) in Ochmann (2004)] but in a different form. A unified expression of the half-space Green's function was also introduced by Ochmann [Eq. (41) in Ochmann (2004)] which is convergent for both mass-like and spring-like impedance but is expressed in z-complex plane. Based on the unified half-space Green's function, a general half-space FMBEM of the infinite plane with impedance boundary condition may also be obtained.

Acknowledgments

The work is supported by grant 11074170 of the National Natural Science Foundation of China and Grant MSVMS201105 of Foundation of the State Key Laboratory of Mechanical System and Vibration.

References

Agrest, M. M. and Maksimov, M. Z. [1971] *Theory of Incomplete Cylindrical Functions and Their Applications* (Springer-Verlag, Berlin).

Bapat, M. S., Shen, L. and Liu, Y. J. [2009] "Adaptive fast multipole boundary element method for three-dimensional half-space acoustic wave problems," *Eng. Anal. Bound. Elem.* **33**, 1113–1123.

Brick, H. and Ochmann, M. [2008] "A half-space BEM for the simulation of sound propagation above an impedance plane," Acoustics '08, Pairs, France, pp. 2417–2422.

Burton, A. J. and Miller, G. F. [1971] "The application of integral equation methods to the numerical solution of some exterior boundary-value problems," *Proc. Royal Soc. London Series A, Mathematical and Physical Sciences*, **323**, 201–210.

Chen, Z. S. and Waubke, H. [2010] "A simple method for computing the green functions of the Helmholtz equation in the two-dimensional impedance half space," *J. Comput. Acoust.* **18**, 1–11.

Chen, J. T. and Chen, K. H. [2004] "Applications of the dual integral formulation in conjunction with fast multipole method in large-scale problems for 2D exterior acoustics," *Eng. Anal. Bound. Elem.* **28**, 685–709.

Chen, Y. H., Chew, W. C. and Zeroug, S. [1997] "Fast multipole method as an efficient solver for 2D elastic wave surface integral equations," *Comput. Mech.* **20**, 495–506.

Cheng, H., Crutchfield, W. Y., Gimbutas, Z., Greengard, L. F., Ethridge, J. F. and Huang, J. *et al.* [2006] "A wideband fast multipole method for the Helmholtz equation in three dimensions," *J. Comput. Phys.* **216**, 300–325.

Coifman, R., Rokhlin, V. and Wandzura, S. [1993] "The fast multipole method for the wave equation: A pedestrian prescription," *Antennas Propag. Mag., IEEE* **35**, 7–12.

Darve, E. and Havé, P. [2004] "Efficient fast multipole method for low-frequency scattering," *J. Comput. Phys.* **197**, 341–363.

Fischer, M., Gauger, U. and Gaul, L. [2004] "A multipole Galerkin boundary element method for acoustics," *Eng. Anal. Bound. Elem.* **28**, 155–162.

Greengard, L. and Rokhlin, V. [1987] "A fast algorithm for particle simulations," *J. Comput. Phys.* **73**, 325–348.

Greengard, L., O'Neily, M. and Pataki, A. [2011] "On the efficient representation of the half-space impedance Green's function for the Helmholtz equation," arXiv:1109.6708.

Gumerov, N. A. and Duraiswami, R. [2009] "A broadband fast multipole accelerated boundary element method for the three dimensional Helmholtz equation," *J. Acoust. Soc. Amer.* **125**, 191–205.

Ingard, U. [1951] "On the reflection of a spherical sound wave from an infinite plane," *J. Acoust. Soc. Amer.* **23**, 329–335.

Kawai, T., Hidaka, T. and Nakajima, T. [1982] "Sound propagation above an impedance boundary," *J. Sound Vib.* **83**, 125–138.

Koc, S. and Chew, W. C. [1998] "Calculation of acoustical scattering from a cluster of scatterers," *J. Acoust. Soc. Amer.* **103**, 721–734.

Koh, I. S. and Yook, J. G. [2006] "Exact closed-form expression of a sommerfeld integral for the impedance plane problem," *IEEE Trans. Antennas Propag.* **54**, 2568–2576.

Kress, R. [1985] "Minimizing the condition number of boundary integral operators in acoustic and electromagnetic scattering," *Quarter. J. Mech. Appl. Math.* **38**, 323–341.

Li, Y. L., White, M. J. and Hwang, M. H. [1994] "Green's functions for wave propagation above an impedance ground," *J. Acoust. Soc. Amer.* **96**, 2485–2490.

Li, Y. L. and White, M. J. [1996] "Near-field computation for sound propagation above ground — Using complex image theory," *J. Acoust. Soc. Amer.* **99**, 755–760.

Li, W. L., Wu, T. W. and Seybert, A. F. [1994] "A half-space boundary element method for acoustic problems with a reflecting plane of arbitrary impedance," *J. Sound Vib.* **171**, 173–184.

Liu, Y. J., Mukherjee, S., Nishimura, N., Schanz, M., Ye, W. and Sutradhar, A. *et al.* [2011] "Recent advances and emerging applications of the boundary element method," *Appl. Mech. Rev.* **64**, article no. 031001.

Liu, Y. J. [2009] *Fast Multipole Boundary Element Method*: *Theory and Applications in Engineering* (Cambridge University Press, Cambridge).

Liu, Y. J. and Nishimura, N. [2006] "The fast multipole boundary element method for potential problems: A tutorial," *Eng. Anal. Bound. Elem.* **30**, 371–381.

Matsumoto, T., Zheng, C., Harada, S. and Takahashi, T. [2010] "Explicit evaluation of hypersingular boundary integral equation for 3D Helmholtz equation discretized with constant triangular element," *J. Comput. Sci. Technol.* **4**, 194–206.

Nemitz, N. and Bonnet, M. [2008] "Topological sensitivity and FMM-accelerated BEM applied to 3D acoustic inverse scattering," *Eng. Anal. Bound. Elem.* **32**, 957–970.

Nishimura, N. [2002] "Fast multipole accelerated boundary integral equation methods," *Appl. Mech. Rev.* **55**, 299–324.

Ochmann, M. [2004] "The complex equivalent source method for sound propagation over an impedance plane," *J. Acoust. Soc. Amer.* **116**, 3304–3311.

Rahola, J. [1996] "Diagonal forms of the translation operators in the fast multipole algorithm for scattering problems," *BIT Numer. Math.* **36**, 333–358.

Saad, Y. [1993] "A flexible inner-outer preconditioned GMRES algorithm," *SIAM J. Scient. Comput.* **14**, 461–469.

Sakuma, T. and Yasuda, Y. [2002] "Fast multipole boundary element method for large-scale steady-state sound field analysis. Part I: Setup and validation," *Acta Acust. United Ac.* **88**, 513–525.

Sarabandi, K., Casciato, M. D. and Koh, I. S. [2002] "Efficient calculation of the fields of a dipole radiating above an impedance surface," *IEEE Trans. Antennas Propag.* **50**, 1222–1235.

Seybert, A. F. and Soenarko, B. [1988] "Radiation and scattering of acoustic waves from bodies of arbitray shape in a three-dimensional half space," *J. Vib. Acoust. Stress Reliab. Des.* **110**, 112–117.

Shen, L. and Liu, Y. J. [2007] "An adaptive fast multipole boundary element method for three-dimensional acoustic wave problems based on the Burton–Miller formulation," *Comput. Mech.* **40**, 461–472.

Thomasson, S. I. [1976] "Reflection of waves from a point source by an impendance boundary," *J. Acoust. Soc. Amer.* **59**, 780–785.

Wenzel, A. R. [1974] "Propagation of waves along an impedance boundary," *J. Acoust. Soc. Amer.* **55**, 956–963.

Wu, H. J., Liu, Y. J. and Jiang, W. K. [2012a] "Analytical integration of the moments in the diagonal form fast multipole boundary element method for 3D acoustic wave problems," *Eng. Anal. Bound. Elem.* **36**, 248–254.

Wu, H. J., Liu, Y. L. and Jiang, W. K. [2012b] "A fast multipole boundary element method for 3D multi-domain acoustic scattering problems based on the Burton–Miller formulation," *Eng. Anal. Bound. Elem.* **36**, 779–788.

Wu, H. J., Liu, Y. J. and Jiang, W. K. [2013] "A low frequency fast multipole boundary element method based on analytical integration of the hypersingular integral for 3D acoustic problems," *Eng. Anal. Bound. Elem.* **37**, 309–318.

Yasuda, Y. and Sakuma, T. [2005] "A technique for plane-symmetric sound field analysis in the fast multipole boundary element method," *J. Comput. Acoust.* **13**, 71–85.

Yasuda, Y., Higuchi, K., Oshima, T. and Sakuma, T. [2012] "Efficient technique in low-frequency fast multipole boundary element method for plane-symmetric acoustic problems," *Eng. Anal. Bound. Elem.* **36**, 1493–1501.

Zheng, C. J., Chen, H. B., Matsumoto, T. and Takahashi, T. [2012] "3D acoustic shape sensitivity analysis using fast multipole boundary element method," *Int. J. Comput. Meth.* **9**, article no. 1240004.